Rheol Acta (2013) 52:529–546
DOI 10.1007/s00397-013-0701-y

ORIGINAL CONTRIBUTION

Microfluidic extensional rheometry using a hyperbolic contraction geometry

Thomas J. Ober · Simon J. Haward · Christopher J. Pipe · Johannes Soulages · Gareth H. McKinley

Received: 8 December 2012 / Revised: 8 March 2013 / Accepted: 18 March 2013 / Published online: 18 May 2013

Abstract Microfluidic devices are ideally suited for the study of complex fluids undergoing large deformation rates in the absence of inertial complications. In particular, a microfluidic contraction geometry can be utilized to characterize the material response of complex fluids in an extensionally-dominated flow, but the mixed nature of the flow kinematics makes quantitative measurements of material functions such as the true extensional viscosity challenging. In this paper, we introduce the 'extensional viscometer-rheometer-on-a-chip' (EVROC), which is a hyperbolically-shaped contraction-expansion geometry fabricated using microfluidic technology for characterizing the importance of viscoelastic effects in an extensionally-dominated flow at large extension rates ($\lambda\dot{\varepsilon}_a \gg 1$, where λ is the characteristic relaxation time, or for many industrial processes $\dot{\varepsilon}_a \gg 1\ \mathrm{s}^{-1}$). We combine measurements of the flow kinematics, the mechanical pressure drop across the contraction and spatially-resolved flow-induced birefringence to study a number of model rheological fluids, as well as several representative liquid consumer products, in order to assess the utility of EVROC as an extensional viscosity indexer.

T. J. Ober · S. J. Haward · C. J. Pipe · J. Soulages · G. H. McKinley (✉)
Department of Mechanical Engineering, Hatsopoulos Microfluids Laboratory, Massachusetts Institute of Technology, Cambridge, MA 02139, USA
e-mail: gareth@mit.edu

T. J. Ober
e-mail: tober@mit.edu

S. J. Haward
Faculdade de Engenharia da Universidade do Porto, Centro de Estudos de Fenómenos de Transporte, Rua Dr. Roberto Frias, 4200-465 Porto, Portugal

Keywords Microfluidic rheometry · Extensional viscosity indexer · High elongation rates · Micro-particle image velocimetry · Flow-induced birefringence

Introduction

Microfluidic devices are invaluable for many rheometric experiments because they can be easily designed to mimic the micron-sized features of geometries that are found in many industrial applications, (e.g., in fiber extrusion spinnerets, ink jet printer nozzles and as model porous media Ferer et al. 2011). Such devices are also inexpensive and easy to fabricate, they require only small sample volumes and allow the rheologist to impose large deformation rates in complex fluids without complications from inertial effects. Large deformation rates may be found, for example, in the chewing of foodstuffs in the mouth, where the closing speed of the jaw may be of order $\mathcal{V} \sim 1\ \mathrm{cm.s}^{-1}$ and the smallest passages between teeth may be $\ell \sim 100\ \mu\mathrm{m}$, making for characteristic deformation rates of at least $\dot{\varepsilon}_c \sim \mathcal{V}/\ell \sim 100\ \mathrm{s}^{-1}$. Furthermore, microfluidic devices can be used to generate mixed flows that have shear as well as extensional components, which are more realistic for many real world applications.

The use of microfluidic technology for rheometry has recently been reviewed by Pipe and McKinley (2009) and Galindo-Rosales et al. (2013). To generate an internal extensional flow, the test fluid typically travels through a converging region or a contraction such that the mean axial velocity u_x of a fluid element changes in the flow direction as the sample travels through the device, (i.e., so that $\partial u_x/\partial x \neq 0$). Careful consideration must be given to the shape of the contraction in order to realize the desired extensional deformation. Many of the earliest studies with

converging geometries utilized abrupt or constant-angle, tapered macroscale contractions (Cogswell 1978; Binding and Walters 1988). The hyperbolically-shaped contraction is unique in that it can be used to impose a nominally constant extension rate along its centerline for a given volumetric flow rate, as discussed by James (1991). It was first studied in an axisymmetric configuration by Everage and Ballman (1978), but the corresponding planar configuration, was first studied only recently by Oliveira et al. (2007). These authors studied the detailed kinematics of planar hyperbolic contraction flows both experimentally and numerically for Newtonian fluids, noting that for creeping flow, the effects of viscous shearing are the dominant contribution to the total pressure drop along the contraction and that it is difficult to isolate purely extensional effects.

For viscoelastic fluids, however, there can be a significant additional elastic contribution to the total pressure drop as a result of the transient elongational flow experienced by the fluid elements passing through the contraction. This facilitates the measurement of an effective extensional viscosity using a hyperbolic contraction device. Many studies using a range of model fluids and viscoelastic constitutive models have been performed to assess the suitability of converging dies for measuring extensional viscosity, typically by attempting to decouple the viscous and elastic contributions to the measured pressure drop (James and Saringer 1982; Rajagopalan 2000; Feigl et al. 2003; Pandey and Lele 2007; Oliveira et al. 2008; Wang et al. 2010; Sousa et al. 2011). In the computational study of Rajagopalan (2000), for example, the Phan-Thien-Tanner (PTT) model was used to predict the pressure field in the flow through both abrupt and tapered contractions, from which an extensional viscosity was calculated using different analytical techniques and compared against the predicted extensional viscosity for the PTT model in a homogeneous extensional flow. In general it was found that the analytical procedures for extracting an extensional viscosity from the inhomogeneous flow field gave results that were in agreement with the true extensional viscosity expected in a homogeneous extensional flow, provided the extension rates were sufficiently large. Furthermore, for the range of PTT model parameters considered, Hencky strains of at most $\varepsilon_H = 4.5$ were required to attain steady state, and with decreasing strain rates, the minimum Hencky strain required to attain steady state decreased. Tamaddon-Jahromi et al. (2011) performed a parametric study using the PTT and the Bautista–Manero models for simulating the flows of worm-like micellar systems in steady shear and homogeneous extensional flows, as well as flow through an abrupt contraction. In this study, it was found that the respective predictions of vortex growth and pressure drop values in the contraction flow differed most between the two models for fluids exhibiting increasing levels of strain hardening in homogeneous extensional flow. Nyström et al. (2012) used the FENE-CR model to study a range of axisymmetric abrupt, hyperbolic and tapered contractions to determine the optimal geometry for generating a constant extension rate along the centerline of the contraction. The hyperbolic geometry was found to be best for imposing a spatially uniform extension rate and no upstream vortices were observed in this geometry. In the numerical study of Afonso et al. (2011), the Oldroyd-B and PTT models were used to simulate flows through axisymmetric and three-dimensional square abrupt contractions at Deborah numbers up to $\mathcal{O}(10^4)$. The formation of upstream vortices was observed as flow rate was increased, along with a transition to unsteady flow at a critical Deborah number and a frequency-doubling behavior with further increases in flow rate ultimately leading to a chaotic regime.

For the experimentalist studying contraction flows, the challenge lies in using kinematic and pressure measurements to extract a quantitative measure of the extensional flow resistance of the test fluid. To illustrate this point, we consider the pressure drop measurements for a range of polyethylene oxide (PEO) solutions in the same Newtonian solvent across a planar hyperbolic contraction-expansion at different low Reynolds number flow rates shown in Fig. 1. For all of the PEO solutions, the pressure drop increases non-linearly with flow rate, and it can be many times larger than the corresponding Newtonian value at a given flow rate. Therefore, it would be valuable to have a method for

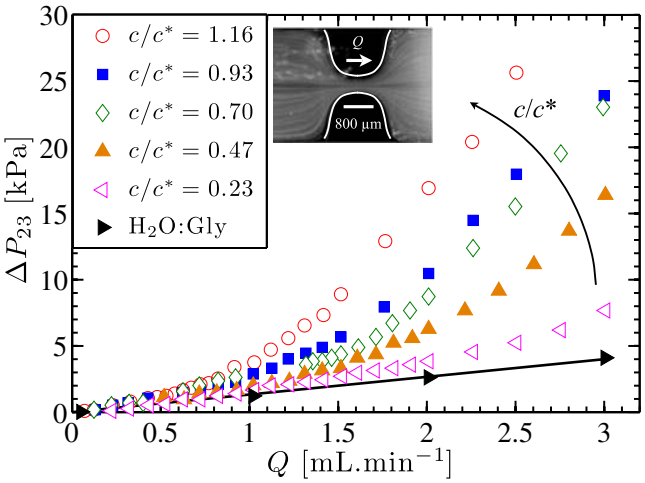

Fig. 1 Measured pressure drop ΔP_{23} across the planar 7.75:1 hyperbolic contraction-expansion as a function of flow rate Q for low viscosity solutions of high molecular weight PEO (2×10^6 g.mol^{-1}, overlap concentration $c^* = 8.58 \times 10^{-4}$ g.mL^{-1}; Sigma–Aldrich) in a water:glycerol solvent ($\mu = 8.2$ mPa.s). The *solid black line* has been added to guide the eye for the results of the Newtonian solvent. Inset figure is a streakline image of the creeping flow ($Re \ll 1$ and $De \ll 1$) through the hyperbolic contraction-expansion (channel thickness $h = 200$ μm, inlet width $w_u = 3100$ μm, throat width $w_c = 400$ μm and contraction length $l_c = 825$ μm)

systematically quantifying the importance of viscoelastic contributions in these total pressure drops in order to quantitatively compare the rheological behavior of different fluids in an extension-dominated mixed flow.

To that end, within the last decade, there have been many experimental studies of extension-dominated mixed flows of non-Newtonian fluids in microfluidic devices. The small length scales of these test geometries facilitate flows at low Reynolds number but large deformation rates, enabling experimentalists to study the importance of viscoelastic effects in high Weissenberg number extensional flows. The viscoelastic flow of polyacrylamide solutions through a series of contraction-expansions has been suggested as a novel way to create a microfluidic rectifier (Groisman and Quake 2004). Recently, Sousa et al. (2012) compared the flow of a Newtonian fluid with a high molecular weight PEO solution in a microfluidic rectifier device composed of a series of hyperbolic contractions and different channel depths, finding that diodicity ratios as high as 6.4 could be achieved using the viscoelastic fluid even at very low Reynolds numbers. The competing roles of fluid inertia and viscoelasticity on the kinematics and pressure drop in the flow of PEO solutions through a planar abrupt contraction were studied by Rodd et al. (2005, 2007). PEO and hydroxyethyl cellulose solutions were used to study the importance of end effects in the pressure drop across a straight microchannel by Kang et al. (2006). They found that for these fluids the dominant contribution to the Bagley correction came from the flow in contraction and expansion regions upstream and downstream of the channel, rather than from the development region in the straight channel itself. Experiments with xanthan gum flowing in a T-channel have also been studied by Bandalusena et al. (2009) and corresponding computational studies have been preformed by Bandalusena et al. (2010). Microfluidic analogues of the four-roll mill have been studied for imposing mixed extensional and shear flows (Hudson et al. 2004; Lee et al. 2007).

Recently, Wang and James (2011) studied the flow of Newtonian and PEO solutions in a planar microfluidic hyperbolic contraction (19:1 contraction ratio) by using both miscible and immiscible, low viscosity Newtonian lubricating fluids to facilitate a more homogeneous elongational flow in the inner viscoelastic fluid. In calibration experiments with a Newtonian fluid, but no lubricating fluid, very good agreement was found between the velocimetry and pressure measurements and analytical predictions based on the lubrication approximation. In the lubricated experiments with a viscoelastic core fluid, the flow was found to be stable only if an immiscible fluid was used as the lubricating fluid. However, the location of the fluid-fluid interfaces was dependent on flow rate and thus flow visualization measurements were necessary to complement the pressure measurement for accurate determination of the extensional viscosity.

Worm-like micellar (WLM) fluids have also been studied in millifluidic and microfluidic extension-dominated flows (Hashimoto et al. 2006; Stone et al. 2006; Pathak and Hudson 2006; Marín-Santibáñez et al. 2009; Haward et al. 2012a; Dubash et al. 2012; Haward and McKinley 2012). Microfluidic devices are well-suited for studies of WLM fluids, because the small length scales can be used to explore the role of non-local effects in the stress field (Masselon et al. 2008). Furthermore, the ability of these fluids to shear band enables the formation of effective lubrication layers at the channel walls, facilitating a plug-like flow in the core of the fluid that can be beneficial for obtaining a more homogeneous extensional flow field in a contraction geometry.

From all of these prior studies, it is clear that for extension-dominated flows in microfluidic devices, viscoelasticity plays a crucial role in the resulting kinematic and stress fields, making determination of the extensional viscosity challenging. Therefore, a valuable complement to pressure and velocimetry measurements are flow-induced birefringence measurements, which can be used to observe the degree of molecular alignment and stretching in material elements as they flow through the device. In certain cases these measurements can be related to the stress difference in the material with a stress-optical rule (Fuller 1990). Such measurements have been used extensively for polymeric and WLM fluids in macroscale geometries, (Fuller 1990; Lerouge and Berret 2010), including contraction flows, (Adams et al. 1965; Han and Drexler 1973a, b; Schuberth and Münstedt 2008). Recent studies of birefringence in microchannels have focused on WLM fluids (Pathak and Hudson 2006; Haward et al. 2012a; Dubash et al. 2012; Haward and McKinley 2012). This is because WLM systems are typically around one hundred times more birefringent than polymeric systems, consequently the small optical path lengths associated with microfluidic devices can still provide a strong enough signal for experimental measurements. In these studies, birefringence and velocimetry measurements were used to characterize the flow instabilities and conformational hysteresis of shear banding WLM fluids undergoing extensional deformations in microfluidic cross-slot geometries.

Typically, studies of extension-dominated flows in microfluidic devices have been limited to model rheological fluids such as dilute polymer solutions and worm-like micellar fluids. Ultimately, it would be desirable to develop a device that can be used with both model fluids and more complex commercially relevant materials to rapidly and quantitatively characterize their behavior in internal, microscale extensional flows, representative of real engineering flows through nozzles and

porous media, for example, as well as flows in the digestive and circulatory systems in the body. In this regard we follow in the spirit of Binding and Walters (1988) who note that "generating a purely extensional flow in the case of mobile liquids is virtually impossible. The most that one can hope to do is to generate flows with a high extensional component and to interpret the data in a way which (hopefully) captures that extensional component in a convenient and consistent way through a suitably defined extensional viscosity and strain rate. The philosophy is not without its difficulties and is somewhat controversial. However, given the practical importance of the subject and the expectation that there will be at least semi-quantitative predictive capacity, it is our contention that the pursuit is eminently worthwhile, especially since there is no alternative if one requires some indication of the extensional viscosity levels in the flow of non-Newtonian elastic liquids."

In this paper, we consider an 'extensional viscometer-rheometer-on-a-chip' (EVROC) for use as a microfluidic extensional viscosity indexer to quantify the rheological behavior of complex fluids in an extension-dominated mixed flow. We combine (1) mechanical pressure drop measurements, with highly-resolved measurements of (2) flow kinematics as well as (3) flow-induced birefringence (FIB) to understand the rheological response of a range of Newtonian and non-Newtonian sample fluids to an extension-dominated deformation. The combination of birefringence and velocimetry measurements in microfluidic devices offers the experimental rheologist the ability to obtain spatially resolved measurements of the state of stress as well as the molecular stretching in elastically-dominated flows of complex fluids.

Experimental methods

Channel fabrication and hyperbolic geometry

The microfluidic planar hyperbolic contractions were fabricated in Pyrex using standard wet-etching techniques by RheoSense (San Ramon CA, USA) as described elsewhere (Pipe et al. 2008). The pressure measurements were made with a chip constructed by anodically bonding the Pyrex contraction-expansion to a silicon wafer with four flush mounted microelectromechanical systems (MEMS) based pressure sensors. This fabrication technique, however, produces a chip with an opaque black plane, and therefore it could not be used for flow visualization. Accordingly, a second, transparent contraction-expansion geometry of the same dimensions was fabricated from Pyrex and sealed to a 150 μm thick microscope coverslip to enable direct flow visualization experiments. An optical microscopy image and a schematic diagram of the contraction are shown in Fig. 2, with channel dimensions given in the figure caption.

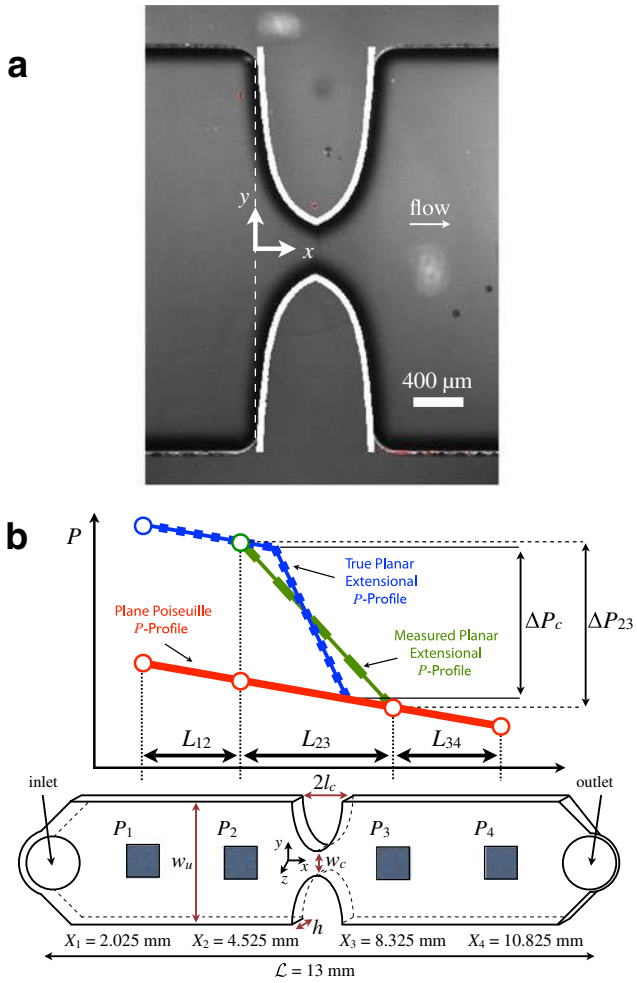

Fig. 2 **a** Optical transmission microscope image of the planar hyperbolic contraction-expansion geometry. Two curves outlining the contraction walls are superimposed on the image. The origin of the experimental coordinate system lies along the contraction centerline and at the contraction inlet as shown by the *dashed white line*. **b** Schematic diagram of the hyperbolic planar contraction and representative pressure profile, showing the coordinate system and variables used throughout the text. The contraction dimensions are $h = 200$ μm, $l_c = 400$ μm, $w_c = 400$ μm and $w_u = 2920$ μm. The *solid squares* indicate the approximate size and location of the flush-mounted MEMS pressure transducers. The schematic depiction is approximately to scale

The throat of the contraction was positioned at the mid-plane of the entire length of the channel ($\mathcal{L} = 13$ mm), but we define the origin of our experimental coordinate system to lie along the contraction centerline and at the beginning of the contraction inlet as shown in Fig. 2a. The hyperbolic contraction is a unique geometry because it can be used, in principle, to impose a constant, nominal extension rate, owing to the fact that its cross-sectional area varies inversely with axial position. Indeed, if the flow is inviscid, or perfect slip at the wall occurs, for example if the flow is lubricated, then $\dot{\varepsilon}_{xx} = \partial u_x/\partial x = const$ for a given volumetric flow

rate. For real fluids, however, the no-slip boundary condition at the wall cannot be circumvented and a more detailed analysis of the kinematics is required.

For the contraction depicted in Fig. 2 having length, l_c, height, h, upstream width, w_u, width at the contraction throat, w_c, the width, $w(x)$, at any x takes the form $w(x) = K/(x_0 + x)$, where $x_0 = l_c w_c/(w_u - w_c)$ and $K = x_0 w_u$. Given a constant volumetric flow rate, Q, through the contraction, the average velocity at any x-position is $u_x = Q/hw(x)$, and so the apparent or nominal extension rate, $\dot{\varepsilon}_a$, neglecting any shearing flow induced by the bounding walls is

$$\dot{\varepsilon}_a = \frac{Q}{l_c h}\left(\frac{1}{w_c} - \frac{1}{w_u}\right) \tag{1}$$

The Hencky strain experienced by a fluid element, ε_H, flowing into the contraction is given by the equation

$$\varepsilon_H(x) = \int_0^t \dot{\varepsilon}_a dt' = \ln\left(\frac{w_u}{w(x)}\right) \tag{2}$$

The maximum Hencky strain occurs at the throat of the contraction and is therefore equal to $\varepsilon_H = \ln(w_u/w_c)$. For the specific channel geometry considered here $w_u = 2920\ \mu$m and $w_c = 400\ \mu$m, so the total Hencky strain is $\varepsilon_H = 2$.

Subsequent to the hyperbolic contraction region is a symmetric hyperbolic expansion ($l_c \le x \le 2l_c$). This configuration has been designed to generate a kinematically reversible flow for Newtonian fluids at low Reynolds numbers and thus equal energy dissipation in the contraction and expansion sections. There is a major difference between the contraction and expansion, however, in that the direction of molecular extension is aligned with the flow through the contraction, but perpendicular to the primary flow direction in the expansion.

Experimental techniques

Pressure drop measurements were made with the EVROC, which was fabricated with four inline, $800 \times 800\ \mu\text{m}^2$ MEMS-based pressure transducers along the centerline, following the construction methods described in Baek and Magda (2003). The maximum measurable pressure of the device was $P_{\max} = 40$ kPa, corresponding to the maximum allowable deflection of the membrane of the MEMS transducer. Measurement precision is approximately 100 Pa (0.2 $\%P_{\max}$). The temperature of the chip was controlled by a thermal jacket (RheoSense Inc.), and an F12-ED Refrigerated/Heating Circulator (Julabo Inc.). Before each test, the EVROC contraction geometry was washed with ethanol and deionized water and then a sufficiently large amount of the test fluid was flushed through the contraction to ensure that there were no air bubbles remaining in the contraction. The test fluid was then allowed to rest in the microchannel for around 15 min, to allow the pressure field to equilibrate, after which the baseline pressure was measured. All tests were completed with a 2.5 mL Hamilton Gastight glass syringe (Reno, NV). For a given test fluid, a set of flow rates was selected so as to yield pressure drops spanning the entire dynamic range of the pressure transducers or to maximize the pump flow rate ($Q_{\max} = 5.2$ mL.min^{-1}), whichever occurred first. The sampling period of each flow rate was selected such that the pressure profile attained a steady state value. Typically the lowest flow rates required on the order of minutes to become steady and the highest flow rates required only seconds. Hence, multiple tests were completed for each fluid to determine the necessary duration of each flow rate and to ensure repeatability.

Representative pressure profiles along the microchannel are depicted schematically in Fig. 2b. The line labelled 'Plane Poiseuille P-Profile' represents the hypothetical pressure profile that would be measured without a contraction-expansion using an equivalent microfluidic chip designed for shear rheometry. The profile labelled 'Measured Planar Extensional P-Profile' indicates a typical non-linear profile that is measured using the hyperbolic contraction-expansion geometry. The pressure drop between transducers 2 and 3 is denoted ΔP_{23}. The pressure drop that is of interest for extensional rheology measurements is the pressure drop associated with the contraction alone, ΔP_c, which is somewhat different from ΔP_{23}. This difference arises because the MEMS transducers 2 and 3 are located some distance upstream and downstream of the contraction entrance and exit. This extra distance is a result of fabrication constraints on the minimum relative spacing between each transducer. It also is designed to ensure that both transducers lie far enough up and downstream of the contraction that they are located in regions of the channel where the rectilinear shear flow provides the dominant contribution to the pressure gradient. To calculate the value of ΔP_c, one can use the average of the pressure gradients for $X_1 < X < X_2$ and $X_3 < X < X_4$ to extrapolate the fully-developed shear flow pressure profile in the upstream and downstream channels to the inlet and outlet of the contraction, similar to the analysis of Wang et al. (2010). In making this extrapolation, fully-developed, rectilinear shear flow at low Reynolds number is assumed to dominate between the second transducer and the contraction inlet and between the contraction outlet and the third transducer. Accordingly, under the assumption that any possible inertial contributions to the pressure drop in the contraction region can be neglected, the true pressure drop across the contraction, ΔP_c, is related to the measured pressured drop, ΔP_{23}, by the relation

$$\Delta P_c = \Delta P_{23}\left\{1 - \frac{1}{2}\left(\frac{1}{\mathcal{P}} - 1\right)\frac{L_{23} - 2l_c}{L}\right\} \tag{3}$$

where $L_{23} = 3.8$ mm, $L \equiv L_{12} = L_{34} = 2.5$ mm and $l_c = 400\ \mu$m.

A useful dimensionless pressure coefficient is defined in Eq. 3 as $\mathcal{P} \equiv \Delta P_{23}/\Delta P_{14}$ where ΔP_{14} is the pressure drop between transducers 1 and 4. The pressure coefficient is positive, and for inertialess flow it is less than unity. It is a measure of the relative importance of the pressure drop in the extension-dominated region of the contraction-expansion geometry compared to the overall pressure drop across the entire microchannel. For low Reynolds number flows, this ratio is a constant independent of flow rate for Newtonian fluids, but it can vary with flow rate for non-Newtonian fluids, reflecting the role of viscoelastic effects in the extension-dominated flow through the contraction. Therefore, this pressure coefficient serves as a simple metric by which to gauge the relative importance of viscoelastic effects in the contraction, and its use will be explained in more detail below.

The μ-PIV experiments were performed in a climate-controlled room in which the temperature was 24 ± 1 °C. The flow rate was controlled with a PHD Ultra syringe pump (Harvard Apparatus). For streakline movies the test fluids were seeded at 0.02 wt.% with fluorescent particles of diameter $d_p = 8\ \mu$m (Invitrogen), having excitation/emission wavelengths of 520/580 nm. Images were recorded with a (640 × 480 pixels) CCD camera (Blue FOX, Matrix Vision) and a continuous illumination mercury lamp with peak emission at 532 nm. In order to visualize the entire contraction region, the images were recorded with a low magnification 2×, $NA = 0.06$ objective, corresponding to a depth of measurement, $\delta z_m = 938\ \mu$m, using the formulae in Meinhart et al. (2000). This depth is greater than the channel thickness, $h = 200\ \mu$m, and accordingly flow across the entire channel height was observed. Higher resolution images are readily possible with a high magnification objective, but it is then not possible to observe the full upstream and downstream flow in a single streak image.

The μ-PIV system used in this study has been described elsewhere, (Rodd et al. 2005), and so it is only briefly reviewed here. Velocimetry measurements were taken with a 10 × 0.25 NA objective with the PIV-Cam 14-10 (1376 × 1024 pixels) CCD camera (TSI Instruments,) and a double-pulsed 532 nm Nd:YAG laser. Test fluids were seeded at 0.02 wt.% with monodisperse fluorescent particles of diameter $d_p = 1.1\ \mu$m (Invitrogen). At this magnification, the depth of measurement was $\delta z_m = 47\ \mu$m, and hence roughly one quarter of the contraction thickness was resolved in the velocimetry measurements. Full-field velocity maps were measured at the centerplane of the contraction, and these were ensemble-averaged using a conventional cross-correlation PIV algorithm (TSI Insight software). The x-component of the centerline velocity at a particular x-position was taken as the average of the x-component of the velocity vectors in the middle third of the throat width of the contraction (i.e., $-\frac{w_c}{6} = -67 \le y \le 67 = \frac{w_c}{6}\mu$m). Error bars in the axial velocity profile plot shown in Fig. 5a correspond to the standard deviation of those data points. All post-processing of the velocity vector fields was performed in MATLAB with a script written by the authors.

Measurements of flow-induced birefringence in the hyperbolic contraction geometry were completed using the ABRIO™ microscopy imaging system (CRi, Inc., Woburn, MA) described in Ober et al. (2011). This system acquires a sequence of recorded images with a liquid-crystal-based optical polarizer, to produce spatially-resolved pixelwise measurements of retardance, $\delta(x, y)$, of the imaged specimen or flow field. For microfluidic flow of a complex fluid, this retardance is related to the local degree of stretching and orientation of the macromolecules in the fluid, and assuming the validity of the stress-optical rule it can be used to evaluate the principal stress difference in the material. Additional details are provided in Ober et al. (2011).

Test fluids

Five Newtonian calibration fluids of different dynamic viscosities, μ, but similar densities, ρ, were first studied. Deionized water was used for flow visualization experiments, and two mixtures of water and glycerol and two silicone-based calibration oils of different viscosities (S60 and N1000, Cannon Inst. Co) were used for pressure calibration measurements in the EVROC device. The rheological properties of these fluids are listed in Table 1. This selection of Newtonian fluids allowed for pressure measurements over nearly eight decades of Reynolds number ($10^{-5} < Re_0 < 10^3$).

The model non-Newtonian fluids studied were 3000 ppm (2×10^6 g. mol^{-1}) polyethylene oxide (PEO) in 34:66 wt% water:glycerol, and the same shear-banding worm-like micellar solution, consisting of 100 mM cetylpyridinium chloride (CPyCl) (Alfa Aesar) and 60 mM sodium salicylate

Table 1 Newtonian fluid properties at 25 °C

Fluid	ρ [kg/m^3]	μ [Pa.s]
Deionized H_2O	1000	0.001
44:56 wt% H_2O:Gly	1130	0.0085
34:66 wt% H_2O:Gly	1160	0.0122
S60 oil	877	0.102
N1000 oil	846	2.0

Viscosities measured with a cone-and-plate rotational rheometer.

(NaSal) (Alfa Aesar) in de-ionized water, that was studied by Ober et al. (2011) and Haward et al. (2012a). This system exhibits single-mode Maxwellian behavior in small amplitude oscillatory shear (SAOS). Above shear rates $\dot{\gamma} > 0.5\ s^{-1}$ this fluid exhibits a pronounced stress plateau, a feature which is indicative of shear banding (Cates and Fielding 2006). Other commercial fluids that were studied include Herbal Essence shampoo (Procter & Gamble) containing the surfactants sodium dodecyl sulfate (SDS) and sodium laureth sulfate (SLES), DayQuil (Vicks) containing waterborne carboxymethycellulose thickener and, finally, sweet chili sauce (Thai Kitchen) containing xanthan gum. The sweet chili sauce was first filtered to remove food particulates and this filtrate showed features of a critical gel in small amplitude oscillatory shear. The flow curves of these fluids were measured using a cone-and-plate geometry on a DHR3 rheometer (TA Instruments) and are shown in Fig. 3.

All of these fluids exhibited a shear-thinning regime which has been fit with the power-law model (Bird et al. 1987), for which the shear viscosity is given by $\eta = m\dot{\gamma}^{n-1}$, where m is the consistency index and n is the dimensionless exponent. The rheological properties of the test fluids

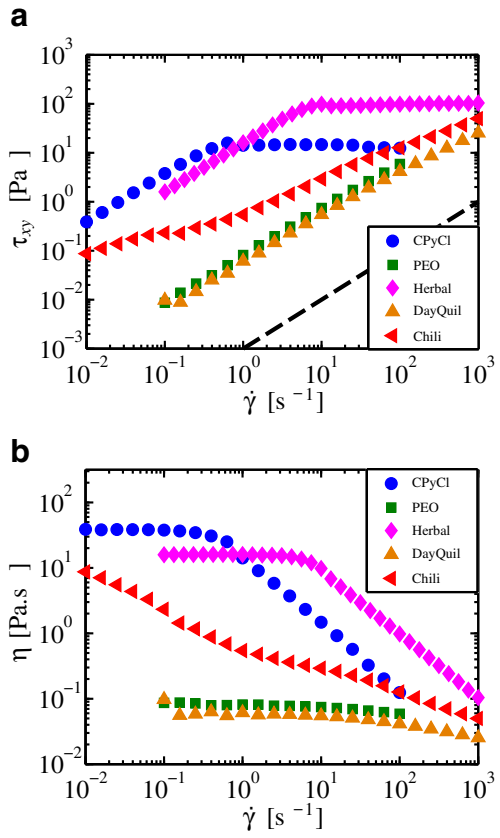

Fig. 3 Steady flow curves of the non-Newtonian test fluids at 25 °C measured with a cone-and-plate rotational rheometer. The *dashed line* shows the stress/shear rate relationship for a Newtonian fluid with $\mu = 10^{-3}$ Pa.s

Table 2 Non-Newtonian fluid properties at 25 °C measured with a cone-and-plate rotational rheometer

Fluid	ρ [kg/m^3]	η_0 [Pa.s]	G_0 [Pa]	λ [s]	m [Pa.s^n]	n
CPyCl:NaSal	1000	40	26	1.5	15	0.01
PEO	1160[a]	0.080		0.076[b]	0.080	0.92
Herbal Essence	1000[a]	15	240	0.062	86	0.027
DayQuil	1000[a]	0.06		0.021[b]	0.1	0.8
Chili Sauce	1000[a]	–		0.56	0.83	0.57

[a]Assumed.

[b]Measured using a capillary break-up extensional rheometer (CaBER).

are given in Table 2. The linear viscoelastic properties of the CPyCl:NaSal solution and the Herbal Essence fluid were obtained by fitting a single mode Maxwell model to the storage and loss moduli measured in SAOS. The relaxation times of the PEO solution and DayQuil were measured using a capillary break-up extensional rheometer (CaBER) (McKinley and Tripathi 2000). Because the chili sauce exhibited a yield stress, its relaxation time was not measured with CaBER, but instead was taken to be the inverse of the cross-over frequency in SAOS.

Dimensional analysis

The relative importance of inertial effects in the device compared to viscous effects is quantified by the Reynolds number

$$Re_0 = \frac{\rho d_h l_c \dot{\varepsilon}_a}{\eta_0} \tag{4}$$

where ρ is the fluid density and η_0 is the zero-shear-rate viscosity of the test fluid, or equivalently the dynamic viscosity, μ, if the fluid is Newtonian. For the flow in the hyperbolic contraction, we take as the characteristic length scale the hydraulic diameter defined at the throat of the contraction as $d_h = 2hw_c/(h + w_c) = 267\ \mu$m. The hydraulic diameter is the most appropriate length scale because it accounts for the two-dimensionality of the channel cross-section, being calculated from both the height and width of the contraction simultaneously. The characteristic velocity is taken to be $U_{char} = l_c\dot{\varepsilon}_a$, which reflects the *change* in the average velocity from the inlet to the throat of the contraction. For large contraction ratios, however, the magnitude of the change in the velocity through the contraction is of the same order as the average velocity at the throat of the contraction (for the contraction used in this study $Q/hw_c = 1.16l_c\dot{\varepsilon}_a$). From either viewpoint $U_{\text{char}} = l_c\dot{\varepsilon}_a$ is the most appropriate velocity scale for defining the Reynolds number for the contraction used in this study.

Table 3 Range of dimensional and dimensionless parameters explored in this study

Fluid	$\dot{\varepsilon}_a$ [s^{-1}]	Re_0	De_a	El_0
H_2O	$10^2 - 10^3$	$10^2 - 10^3$	–	–
S60	$1 - 10^2$	$10^{-2} - 1$	–	–
N1000	$0.1 - 10$	$10^{-5} - 10^{-3}$	–	–
CPyCl	$0.1 - 10^2$	$10^{-7} - 10^{-4}$	$0.1 - 10^2$	6.5×10^5
PEO	$10 - 10^2$	$10^{-3} - 1$	$0.1 - 10^2$	66
Herbal Ess.	$0.1 - 10^2$	$10^{-6} - 10^{-3}$	$10^{-2} - 10$	1.4×10^4
DayQuil	$10 - 10^3$	$10^{-2} - 1$	$0.1 - 10$	12
Chili Sauce	$10 - 10^3$	–	$1 - 10^2$	–

The Deborah number is defined as the ratio of the fluid relaxation time to a time scale of observation. For the steady converging flow in the EVROC, this is taken as the time required for a material element to travel through the contraction, which is proportional to $\dot{\varepsilon}_a^{-1}$, as defined in Eq. 1. Accordingly, the apparent or nominal Deborah number, De_a, based on Eq. 1 is defined

$$De_a = \lambda \dot{\varepsilon}_a \tag{5}$$

The elasticity number, which characterizes the relative importance of elastic stresses to inertial stresses is defined as

$$El_0 = \frac{De_a}{Re_0} = \frac{\lambda \eta_0}{\rho l_c d_h} \tag{6}$$

The range of magnitudes of these dimensionless groups experimentally realized in the study of flow through a hyperbolic contraction are given in Table 3. For all the fluids, $El_0 \gg 1$, indicating that in the experiments with non-Newtonian fluids discussed below inertial stresses were not of importance.

Flow of Newtonian fluids

Pressure measurements

Experimentally measured pressure profiles for the N1000 calibration fluid are shown in Fig. 4a as the flow rate is progressively increased. The flow is viscously dominated and the profiles are self-similar with a pressure drop $\Delta P_{23} \sim \dot{\varepsilon}_a$. For a Newtonian fluid at $Re_0 < 1$, the value of pressure coefficient, $\mathcal{P}^N \approx 0.71$, shown in the inset plot of Fig. 4a, is independent of the viscosity or flow rate, and only a function of the channel geometry. The pressure drop across the contraction alone, ΔP_c is calculated using Eq. 3. The values of the dimensionless pressure drop $\Delta P_c / \mu \dot{\varepsilon}_a$ measured with all Newtonian test fluids are plotted against Reynolds number in Fig. 4b. The onset of inertially-driven secondary

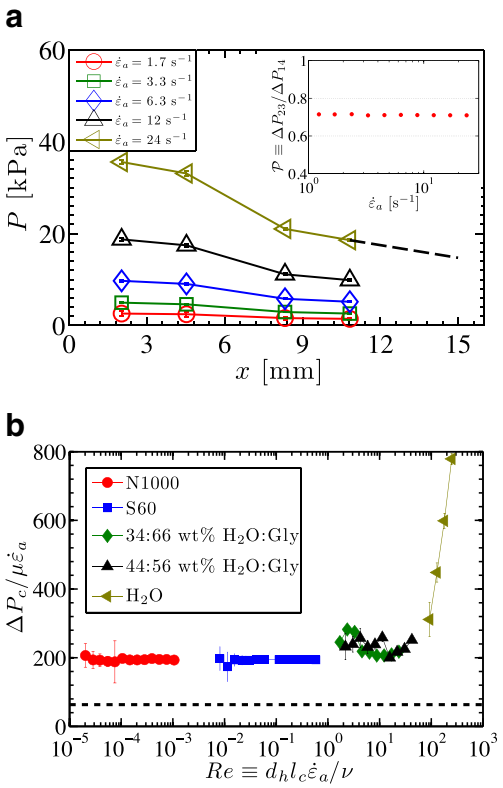

Fig. 4 **a** Pressure measurements as a function of streamwise distance along the microchannel at different $\dot{\varepsilon}_a$ for the N1000 calibration oil. The *dashed line* indicates the anticipated pressure gradient in the downstream section of the channel based on Eq. 16 for a Newtonian fluid ($n = 1$) of the same viscosity as the N1000 calibration oil given in Table 1 ($m = \mu = 2.0$ Pa.s). The inset plot shows the evolution of the pressure coefficient, $\mathcal{P}$, defined for Eq. 3 in the text above. **b** Measured dimensionless pressure drop for Newtonian fluids at varying Reynolds number. The *dashed horizontal line* indicates the anticipated dimensionless pressure drop based on Eq. 8

flow begins around $Re_0 \approx 10$, coinciding with a non-linear increase in ΔP_c with increasing $\dot{\varepsilon}_a$.

The governing equations for the steady flow of an incompressible Newtonian fluid through the contraction geometry are the continuity equation, $\nabla \cdot \vec{v} = 0$, and the steady Navier-Stokes equation, $\rho \vec{v} \cdot \nabla \vec{v} = -\nabla p + \mu \nabla^2 \vec{v}$, with the no-slip boundary condition on the walls. The inertial non-linearity in the momentum equation requires the exact equations to be solved numerically (Oliveira et al. 2007), but for the case of highly viscous Newtonian flow kinematics in the contraction, the momentum equation can be simplified to obtain an approximate solution using the lubrication approximation, provided $Re_0 \frac{w_u}{l_c} \ll 1$. Since $w(x) \geq l_c > h$, we approximate the governing momentum equation by the equation for two-dimensional Stokes flow which is $\frac{dP}{dx} = \mu \frac{\partial^2 u}{\partial z^2}$. Here p is the pressure, x and z follow the coordinate system given in Fig. 2b and $u = u(x, z)$ is the x-component of the velocity field. Using the lubrication approximation, the relationship

between the pressure gradient and the volumetric flow rate appropriate for $h < w(x)$ is given by

$$\frac{dP_c}{dx} = -\frac{12\mu Q}{h^3 w(x)} = -\frac{12 l_c}{h^2 w(x)}\left(\frac{w_c w_u}{w_u - w_c}\right)\mu\dot{\varepsilon}_a \tag{7}$$

Substituting the expression for $w(x)$, therefore the anticipated pressure drop across the contraction-expansion from $x = 0$ to $x = 2l_c$ is

$$\Delta P_c = 12\left(\frac{l_c}{h}\right)^2\left(\frac{w_u + w_c}{w_u - w_c}\right)\mu\dot{\varepsilon}_a \tag{8}$$

The expected pressure drop given by Eq. 8 for the contraction-expansion used in this study is $\Delta P_c/\mu\dot{\varepsilon}_a = 63$, which is indicated by the dashed horizontal line in Fig. 4b. For $Re_0 \ll 1$, however, experimental pressure measurements give $\Delta P_c/\mu\dot{\varepsilon}_a \approx 200$, hence the 2D lubrication approximation underpredicts the measured pressure drop by roughly a factor of three, for reasons that can be better understood by observing the flow kinematics in the microchannel directly, as discussed below.

Flow kinematics

To understand the discrepancy between the simple two-dimensional calculation of the expected pressure drop across the contraction-expansion given by Eq. 8 and the experimental measurements, we compare the measured axial velocity profile against three different characteristic axial velocity profiles. For the hyperbolically shaped planar contraction in this study, the cross-sectional area is $\mathcal{A}(x) = hw(x) \sim x^{-1}$. Therefore, the simplest expected axial velocity profile is the nominal plug-like centerline velocity $u_{cl}^{1D}(x) = Q/\mathcal{A}(x)$, on which the apparent extension rate is based (i.e., $\dot{\varepsilon}_a = du_{cl}^{1D}/dx$). Thus in the contraction region ($0 \le x \le l_c$), the average axial velocity profile is given by

$$u_{cl}^{1D}(x) = (x_0 + x)\dot{\varepsilon}_a \tag{9}$$

The anticipated centerline velocity in the contraction region consistent with the two-dimensional lubrication approximation from Eq. 7 is given by

$$\tilde{u}_{cl}^{2D}(x) = \frac{3}{2}(x_0 + x)\dot{\varepsilon}_a \tag{10}$$

where the tilde denotes a locally fully developed velocity consistent with the lubrication approximation. Finally, the most accurate centerline velocity is given by the lubrication approximation together with the expression for the velocity field in a rectangular channel of finite aspect ratio, which can be found in White (2006), and for this contraction is

$$\tilde{u}_{cl}^{3D}(x) = K(x)(x_0 + x)\dot{\varepsilon}_a \tag{11}$$

where $K(x)$ is defined

$$K(x) = \frac{48}{\pi^3}\frac{\displaystyle\sum_{j=\text{odd}}^{\infty}\frac{(-1)^{\frac{j-1}{2}}}{j^3}\left[1 - \frac{1}{\cosh\left(\frac{j\pi w(x)}{2h}\right)}\right]}{1 - \frac{192}{\pi^5}\frac{h}{w(x)}\displaystyle\sum_{j=\text{odd}}^{\infty}\frac{\tanh\left(\frac{j\pi w(x)}{2h}\right)}{j^5}} \tag{12}$$

The expected velocity profiles in the expansion region are mirror images of the profiles in the contraction due to the channel symmetry. Upstream of the contraction inlet ($x < 0$), the cross-sectional area is constant, so the approximate velocities to be matched to these profiles are

$$\begin{aligned} u_{cl}^{1D}(x < 0) &= x_0\dot{\varepsilon}_a \\ u_{cl}^{2D}(x < 0) &= \frac{3}{2}x_0\dot{\varepsilon}_a \\ u_{cl}^{3D}(x < 0) &= K_0 x_0\dot{\varepsilon}_a \end{aligned} \tag{13}$$

where K_0 is defined

$$K_0 = \frac{48}{\pi^3}\frac{\displaystyle\sum_{j=\text{odd}}^{\infty}\frac{(-1)^{\frac{j-1}{2}}}{j^3}\left[1 - \frac{1}{\cosh\left(\frac{j\pi w_u}{2h}\right)}\right]}{1 - \frac{192}{\pi^5}\frac{h}{w_u}\displaystyle\sum_{j=\text{odd}}^{\infty}\frac{\tanh\left(\frac{j\pi w_u}{2h}\right)}{j^5}} \tag{14}$$

For the microchannel used in this study, $K_0 = 1.567$.

The expected axial velocity profiles in the contraction-expansion region given by Eqs. 9, 10 and 11 are compared with the centerline velocity measured using μ-PIV in Fig. 5a. Although the measured profile is qualitatively described by $\tilde{u}_{cl}^{3D}(x)$, it differs from the lubrication solution in two ways. Firstly, the measured centerline velocity profile begins to exceed the anticipated profile starting roughly three contraction lengths upstream of the contraction inlet, as indicated by the horizontal black arrow in Fig. 5a. This initial deviation can be attributed to the abruptness of the contraction seen in Fig. 2a. The importance of sudden changes in cross-section on the kinematics and pressure field in viscously-dominated flows through microfluidic devices was also previously noted in Oliveira et al. (2007). Secondly, the measured velocity exceeds $\tilde{u}_{cl}^{3D}(x)$ in the contraction region ($0 \le x \le 2l_c$), due to a "scalloping" feature of the wet etching process which causes the idealized sharp corners to in fact be rounded so that the cross-sectional area of the channel in the contraction region is 10–20 % less than the anticipated rectangular cross-sectional area. The true extension rate $\dot{\varepsilon}_t$ experimentally realized in the hyperbolic contraction can be calculated from the slope of the best-fit line to the measured velocity profile in the contraction region, and the resulting values are plotted against the nominal extension rate $\dot{\varepsilon}_a$ given by Eq. 1 in Fig. 5b. The true extension rate is roughly 66 % greater than the nominal value based on a linear regression to the measured extension

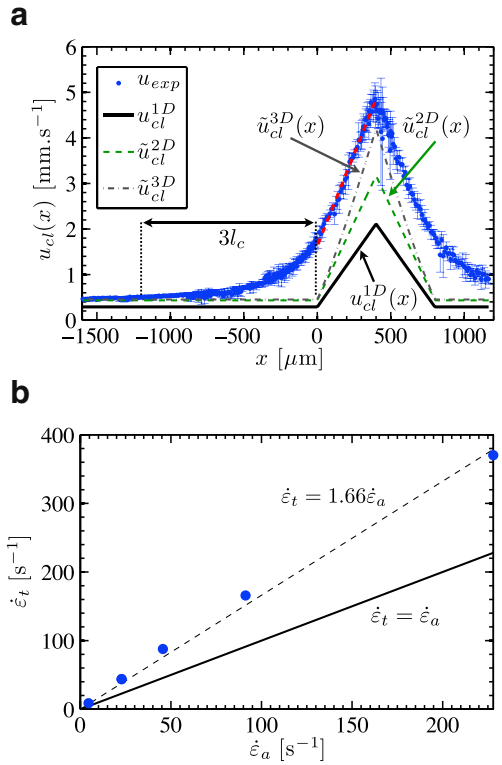

Fig. 5 **a** Experimentally measured (u_{exp}) and anticipated velocity profiles along the centerline of the contraction $u_{cl}(x) = u(x, 0, 0)$ in a Newtonian fluid at $Q = 10$ μL/min, $Re_0 \simeq 0.5$. The *dashed solid line* is the linear best-fit to the measured velocity profile in the converging section of the contraction ($0 \leq x \leq l_c$) whose slope equals the experimentally realized extension rate in the contraction, $\dot{\varepsilon}_t$. **b** True extension rate $\dot{\varepsilon}_t$ determined from the slope of the best-fit line to the measured velocity profile as a function of the imposed $\dot{\varepsilon}_a$. The *solid line* indicates the ideal result of $\dot{\varepsilon}_t = \dot{\varepsilon}_a$, whereas the *dashed line* indicates the result of a least squares fit to the measured extension rate given by the equation $\dot{\varepsilon}_t = 1.66\dot{\varepsilon}_a$

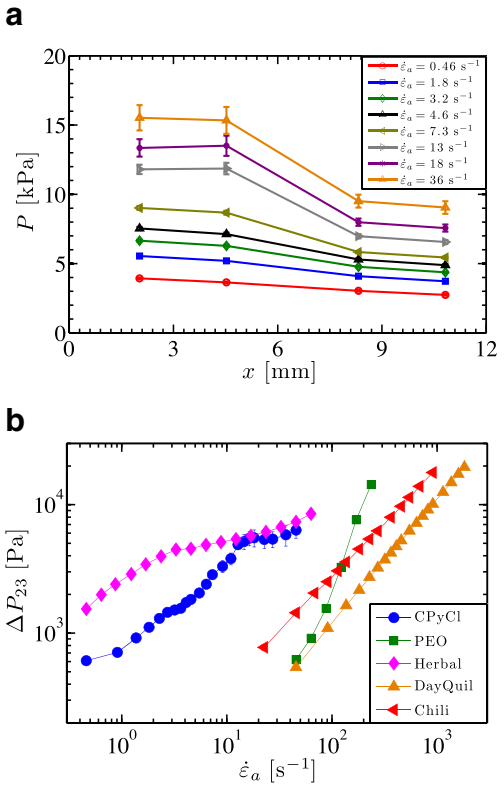

Fig. 6 Pressure measurements in the microfluidic contraction at different nominal extension rates for the 100 : 60 mM CPyCl:NaSal system. **a** Measured pressure as a function of streamwise distance along the microchannel. **b** Measured pressure drop ΔP_{23} for each fluid as a function of the nominal extension rate

rate. These discrepancies between the measured and anticipated kinematics reveal why the lubrication approximation cannot accurately predict the measured pressure drop shown in Fig. 4b. The precise form and extent of the deviations can only be understood using full 3D finite volume simulations, which will be considered in future work.

Flow of non-Newtonian fluids

Pressure measurements

Measured pressure profiles for one of the non-Newtonian test fluids are shown in Fig. 6a. As in the Newtonian case, the dominant contribution to the overall pressure drop in the entire microchannel is ΔP_{23}, and this quantity is plotted in Fig. 6b as a function of nominal extension rate for each fluid tested. This apparent flow curve of pressure drop verses flow rate, however, does not provide an immediately useful metric of the contribution of viscoelastic effects in this mixed flow. One possible metric for quantifying these effects in the contraction is the 'excess pressure drop' (EPD) (Aguayo et al. 2008), which is the ratio of the pressure drop across the contraction for a non-Newtonian fluid to the pressure drop for a Newtonian fluid with the same shear viscosity at a given flow rate. With the exception of Boger fluids (whose shear viscosity is constant), the shear viscosity of most non-Newtonian fluids is rate dependent, and therefore without assuming a constitutive relationship for the shear viscosity of the fluid (e.g., a power-law model as utilized in this work) the calculation and interpretation of the EPD for most viscoelastic materials is ambiguous. An alternative metric for gauging the relative importance of non-Newtonian effects is the pressure coefficient $\mathcal{P} \equiv \Delta P_{23}/\Delta P_{14}$, that was introduced previously in Eq. 3. This quantity is plotted in Fig. 7a and has the advantage that it is based on the uncorrected pressure drop measurements alone and therefore its value can be determined unambiguously. As the fractional contribution of the pressure drop in the contraction to the overall pressure drop in the entire channel increases, the viscoelastic resistance to stretching

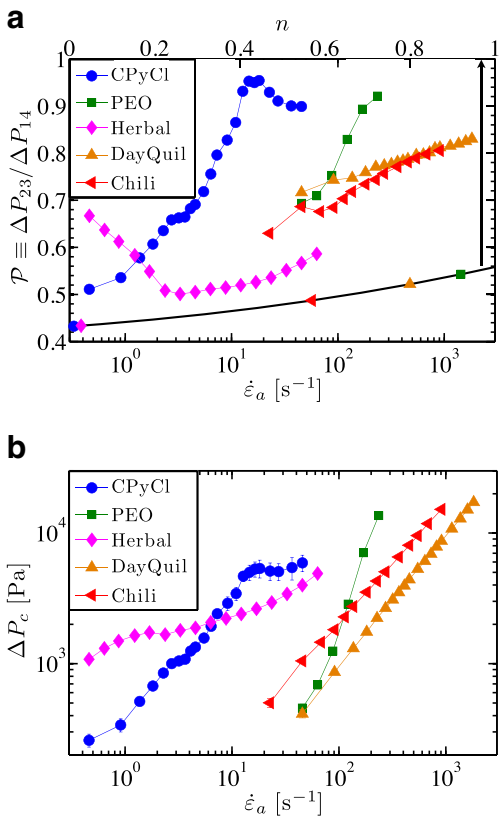

Fig. 7 **a** Pressure coefficient plot for different fluids. The *black curve* corresponds to the minimum predicted value of the pressure coefficient for a power-law fluid with index $0 \leq n \leq 1$ using Eq. (18). Each of the five points on the curve indicates the predicted minimum value of $\mathcal{P}$ corresponding to the value of n for each test fluid listed in Table 2. **b** Corrected pressure drop ΔP_c for each test fluid using Eq. 3

becomes increasingly important and the pressure coefficient $\mathcal{P}$ approaches unity.

It is important to note that for the non-Newtonian test fluids the value of $\mathcal{P}$ may be lower than the respective value for Newtonian fluids, and also that the value does not necessarily asymptote to a constant value at low flow rates. Therefore, it is helpful to make an estimate of the value of $\mathcal{P}$ at the limiting flow rates for which viscous shear effects would constitute the predominant contribution to the pressure drop. It is common to assume that the overall pressure drop in the device can be decomposed as $\Delta P_c = \Delta P_e + \Delta P_v$, whereby the total pressure drop is the superposition of a viscoelastic component ΔP_e and a viscous component ΔP_v due to shearing at the walls, (Cogswell 1972). Without complementary numerical simulations, however, it is difficult to ascertain the viscous contribution to the pressure drop with great precision, but for the flow of a shear-thinning non-Newtonian fluid one can estimate the value of ΔP_v using the phenomenological power-law model (Bird et al. 1987) provided the flow is inertialess and the shear stresses in the fluid are independent of net accumulated strain. This approach for calculating ΔP_v is consistent with other recent analyses for planar contraction flows (Wang et al. 2010). Since the thickness of the hyperbolic contraction flow channel is always less than its width, $h < w_c < w_u$, in our analysis we assume that the dominant velocity gradient will be across the channel height (i.e., in the z-direction), and therefore in the 2D approximation, velocity gradients across the channel width (i.e., in the y-direction) are neglected. For a power law fluid (denoted PL), the resulting pressure gradient due to the viscous shearing component of the flow is related to the nominal extension rate $\dot{\varepsilon}_a$ by the equation

$$\frac{dP_v^{PL}}{dx} = -2^{n+1}\left(\frac{2n+1}{n}\right)^n\left(\frac{l_c}{h}\right)^n\left(\frac{w_c w_u}{w_u - w_c}\right)^n \frac{m\dot{\varepsilon}_a^n}{hw(x)^n} \tag{15}$$

Upstream and downstream of the contraction, $w(x) = w_u$, and thus the magnitude of the pressure gradient in these regions of the channel is constant with value

$$\frac{\Delta P_v^{PL}}{\Delta x} = 2^{n+1}\left(\frac{2n+1}{n}\right)^n\left(\frac{l_c}{h}\right)^n\left(\frac{w_c}{w_u - w_c}\right)^n\left(\frac{1}{h}\right) m\dot{\varepsilon}_a^n \tag{16}$$

The approximate contribution to the pressure drop across the contraction and expansion from $x = 0$ to $x = 2l_c$ due to viscous shear stresses is found by integration of Eq. 15 to be

$$\Delta P_{c,v}^{PL} = \frac{2^{n+2}}{n+1}\left(\frac{2n+1}{n}\right)^n\left(\frac{l_c}{h}\right)^{n+1} \times \left\{\left(\frac{w_u}{w_u - w_c}\right)^{n+1} - \left(\frac{w_c}{w_u - w_c}\right)^{n+1}\right\} m\dot{\varepsilon}_a^n \tag{17}$$

In the limiting case of a Newtonian fluid, $m = \mu$ and $n = 1$, and Eq. 17 reduces to the result for simple 2D plane Poiseuille flow in Eq. 8. Therefore, the estimated value of $\mathcal{P}$ for a power-law fluid is

$$\mathcal{P}^{PL} = \frac{\frac{\Delta P_v^{PL}}{\Delta x}(L_{23} - 2l_c) + \Delta P_{c,v}^{PL}}{\frac{\Delta P_v^{PL}}{\Delta x}(L_{14} - 2l_c) + \Delta P_{c,v}^{PL}} \tag{18}$$

where L_{23} and L_{14} are the distances between transducers 2 and 3, and 1 and 4 respectively. The result given in Eq. 18 is independent of m and $\dot{\varepsilon}_a$, but depends on the value of the power-law index n. This predicted variation in the pressure coefficient for power-law fluids, $\mathcal{P}^{PL}(n)$ is shown as the black curve in Fig. 7a for index values in the range $0 \leq n \leq 1$. The curve represents a lower bound for the pressure ratio, because it does not account for any elastic contribution to the pressure drop and it is based on only a 2D approximation to the flow. Even for a Newtonian fluid, the prediction

of Eq. 18 is $\mathcal{P}^{PL}(n = 1) = 0.56$, which is lower than the typically observed experimental value of $\mathcal{P}^{N} \approx 0.71$. This remaining difference arises from the three dimensional effects in the flow field. Nevertheless, the utility of the dimensionless pressure coefficient $\mathcal{P}$ lies in the fact that it is a primary measure of the relative importance of viscoelastic contributions to the stresses which can be evaluated independently of the constitutive model of the fluid. Indeed, in assessing the value of $\mathcal{P}$ with increasing $\dot{\varepsilon}_a$, it becomes clear that the pressure profiles for the non-Newtonian fluids differ qualitatively from the Newtonian profiles in Fig. 4b, and the contribution of viscoelastic effects generally increases with increasing flow rates for the non-Newtonian test fluids. The two exceptions to this general trend occur for the CPyCl system and Herbal Essence shampoo which both exhibit strongly shear thinning viscosities. For the CPyCl system, the small drop in the pressure coefficient coincides approximately with the onset of a time-varying flow, which affects the pressure profile along the entire channel. For the shampoo, the initial decrease in the pressure coefficient for $\dot{\varepsilon}_a < 3\ \mathrm{s}^{-1}$ results from shear thinning that becomes more important as the flow rate increases. Because of this thinning, the estimate for the minimum pressure coefficient (based on the power-law model) becomes increasingly accurate. The eventual increase in the pressure coefficient indicates that viscoelasticity dominates the pressure drop across the contraction with increasing values of $\dot{\varepsilon}_a$.

The apparent extensional viscosity in an elongational flow is

$$\eta_{E,a} \equiv \frac{N_1}{\dot{\varepsilon}_a} \tag{19}$$

where $N_1 \equiv \tau_{xx} - \tau_{yy}$ is the first normal stress difference. An approximate measure for the value of N_1 can be determined from the elastic contribution to the pressure drop (after subtracting the viscous contribution), $\Delta P_e = \Delta P_c - \Delta P_{c,v}^{PL}$ and then calculated using the following energy argument. For a two-dimensional, incompressible flow, the continuity equation requires that $\dot{\varepsilon}_{xx} = -\dot{\varepsilon}_{yy}$ at each point in the flow. Furthermore, the net rate of work per unit volume associated with a purely extensional deformation is $\dot{\mathcal{W}}''' = \tau_{xx}\dot{\varepsilon}_{xx} + \tau_{yy}\dot{\varepsilon}_{yy}$, or equivalently

$$\frac{D}{Dt}\left(\frac{\partial \mathcal{W}}{\partial \mathcal{V}}\right) = \left(\tau_{xx} - \tau_{yy}\right)\dot{\varepsilon}_{xx} \tag{20}$$

where $\mathcal{V}$ denotes a unit volume. The incremental work must be equal to the external mechanical work acting on the material, $\partial \mathcal{W} = -P\partial \mathcal{V}$ where P is pressure, or alternatively $\partial \mathcal{W}/\partial \mathcal{V} = -P$. Substituting this result and the definition into Eq. 20 and equating $\dot{\varepsilon}_{xx} = \dot{\varepsilon}_a$, one obtains $DP/Dt = -N_1\dot{\varepsilon}_a$. Integration of this equation across the length of the contraction under the assumption that N_1 is constant and using the result of Eq. 2, one obtains $N_1 = \Delta P/\varepsilon_H$, and hence the approximate viscoelastic contribution to the apparent extensional viscosity for fully developed extensional flow in the hyperbolic contraction is

$$\eta_{E,a} = \frac{1}{\varepsilon_H}\frac{\Delta P_e}{\dot{\varepsilon}_a} \tag{21}$$

This result has previously been derived in Collier et al. (1998) and it is only valid for an ideal planar elongational flow, provided the value of N_1 is constant for the entire duration of the deformation. Such an assumption does not capture the variation in the normal stresses with net accumulated strain, $\varepsilon_H(x)$, and it also neglects experimental transients. Furthermore, this derivation is only appropriate for a flow field in which the net accumulated Hencky strain ε_H is independent of the streamline followed by a material element in the flow, or equivalently for the contraction here $\varepsilon_H(x, y, z) = \varepsilon_H(x)$. Note that the expression for $\eta_{E,a}$ given by Eq. 21 is specific to the contraction-expansion geometry used here, and that it differs from the expression for extensional viscosity given for the cross-slot geometry studied by Haward et al. (2012a). This difference arises because the cross-slot flow contains a stagnation point at which the theoretical Hencky strain diverges and the net accumulated strain varies across streamlines. Accordingly, it is not possible to calculate a unique value of N_1 for the entire flow field in the cross-slot, but only an average value. This average value is taken to be approximately equal to the measured excess pressure drop $N_1 \approx \Delta P_{\mathrm{excess}}$. Ultimately, however, the two respective expressions for apparent extensional viscosity are consistent, because they are based on the same definition for $\eta_{E,a}$ given by Eq. 19.

To evaluate $\eta_{E,a}(\dot{\varepsilon}_a)$, the corrected pressure drop ΔP_c must first be determined using Eq. 3. The values of ΔP_c are plotted against $\dot{\varepsilon}_a$ in Fig. 7b for each fluid. The apparent first normal stress difference and extensional viscosity, calculated from Eq. 21 (based on the corrected elongational contribution to the pressure drop ΔP_e), are shown in Fig. 8. For all fluids, the apparent first normal stress difference $N_{1,a}$ increases with $\dot{\varepsilon}_a$. When $N_{1,a}$ is normalized by $\dot{\varepsilon}_a$ to calculate the apparent extensional viscosity defined in Eq. 21, three classes of response emerge. The DayQuil (carboxymethycellulose) and chili sauce (xanthan gum) both exhibit a nearly constant value of $\eta_{E,a}$, whereas the two surfactant systems (CPyCl and shampoo) show extensional thinning. Lastly, the PEO system shows extensional-thickening, similar to the behavior of the highest concentration PEO solutions shown in Fig. 1, for which the measured pressure drop increases superlinearly with flow rate.

The Trouton ratio is defined as the ratio of the extensional viscosity to the shear viscosity, and for a planar elongational flow for simple fluids at small extension rates this limiting value is $Tr_{\dot{\varepsilon}\to 0} \equiv \frac{\eta_E}{\eta_0} = 4$. In our experiments, however,

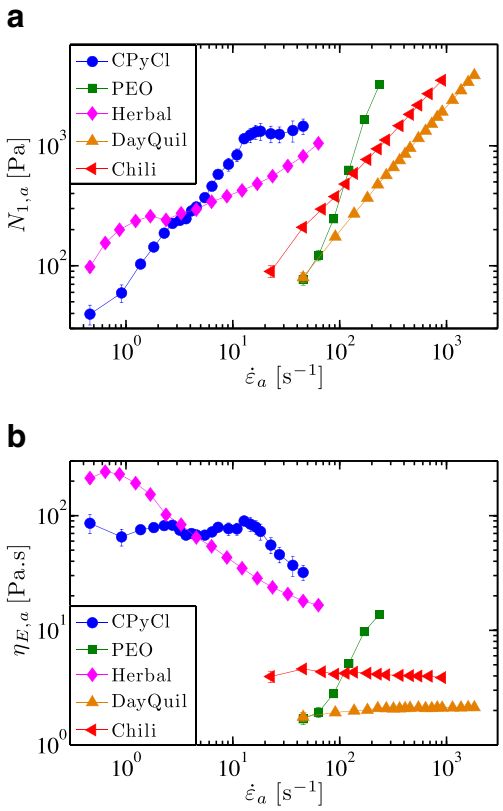

Fig. 8 Calculated values of (**a**) apparent normal stress difference $N_{1,a} = \Delta P_e/\varepsilon_H$ and (**b**) apparent extensional viscosity $\eta_{E,a}$ based on Eq. 21

with the exception of the CPyCl system, the Trouton ratios are notably higher, and their values based on the zero-shear-rate viscosities given in Table 2 at the smallest values of $\dot{\varepsilon}_a$ for each fluid are (a) CPyCl: $Tr \approx 2$, (b) PEO: $Tr \approx 22$, (c) Herbal Essence: $Tr \approx 14$, (d) DayQuil: $Tr = 29$. Such large Trouton ratios have also been reported previously for flow through a hyperbolic contraction, (Wang et al. 2010). It is important to recall that this simple analysis assumes an ideal fully-developed planar elongational flow, whereas the apparent extensional-thinning/thickening behavior and the experimental values of the Trouton ratio are based on measurements of a transient extension-dominated mixed flow. These metrics are therefore best considered as a relevant measure of viscoelastic resistance to stretching in a mixed flow that is characteristic of what would be encountered in an industrial application (such as flow through a nozzle), but not in an ideal homogeneous extensional flow.

Flow kinematics

The deviations between the flow kinematics of the non-Newtonian test fluids in the EVROC device and those expected in an ideal homogeneous extensional flow can be investigated with velocimetry measurements. Accordingly, streakline images for all non-Newtonian test fluids are shown together with complementary pseudocolor optical retardance images of the flow-induced birefringence in Fig. 9. The experimental extension rates measured at the contraction mid-plane have been determined from the slope of a linear regression to the centerline axial velocity profiles along the length of the contraction as discussed previously for Newtonian fluids (*cf.* Fig. 5). The true extension rate, $\dot{\varepsilon}_t$, realized experimentally is plotted against the nominal extension rate, $\dot{\varepsilon}_a$, in Fig. 10.

For most of the test fluids, at least two qualitatively different regimes of behavior are observed with increasing flow rate. At sufficiently small rates, $De_a < \mathcal{O}(1)$, all of the non-Newtonian fluid systems exhibit kinematics that are qualitatively similar to the behavior seen at low Reynolds number in Newtonian fluids. The true extension rate in the contraction is roughly constant and greater than the nominal value as previously noted for the Newtonian case (*cf.* Fig. 5b). Additionally, the streaklines generally follow the contours of the contraction sidewalls as shown in Fig. 9.

At intermediate rates, $De_a \sim \mathcal{O}(10)$, vortices in the upstream corners of the contraction emerge as is evident for the CPyCl micellar fluid, PEO solution and DayQuil in Fig. 9. The distortion of the streamlines from those observed in the Newtonian case clearly indicates the influence of fluid elasticity on the flow kinematics even at vanishingly small Re_0. Such vortices are well-known to occur in flows of viscoelastic fluids through contractions (Rodd et al. 2005; Rodd et al. 2007). Typically, the presence of vortices also results in the onset of a non-linear dependency of the true extension rate $\dot{\varepsilon}_t$, on the nominal value, $\dot{\varepsilon}_a$ as shown in Fig. 10.

Amongst these fluids, the behavior of the CPyCl worm-like micellar system is unique. For this fluid, at $De_a > \mathcal{O}(1)$, the images presented in Fig. 9a show that the streamlines in the contraction region become increasing constricted near the throat resulting in a nearly constant value of $\dot{\varepsilon}_t$ across approximately one order of magnitude of apparent strain rate, $1 < \dot{\varepsilon}_a < 10$ s^{-1}. This is also reflected in the weak increase in true extension rate $\dot{\varepsilon}_t$ with increasing flow rate shown in Fig. 10. It is the ability of this fluid to shear band (i.e., support localized regions of high shear rate) which causes the value of $\dot{\varepsilon}_t$ to plateau, since the shear bands function effectively as moveable internal slip layers. The narrowing of the streamlines also reduces streamwise curvature, thereby allowing the flow to remain steady up to large values of the apparent Deborah number ($De_a < \mathcal{O}(30)$), before becoming time-varying. In this unsteady regime, measurement of the true extension rate in the contraction was not possible. It is noteworthy that the plateau in the experimentally realized extension rate, $\dot{\varepsilon}_t$ for the CPyCl system roughly occurs conjointly with a plateau in the

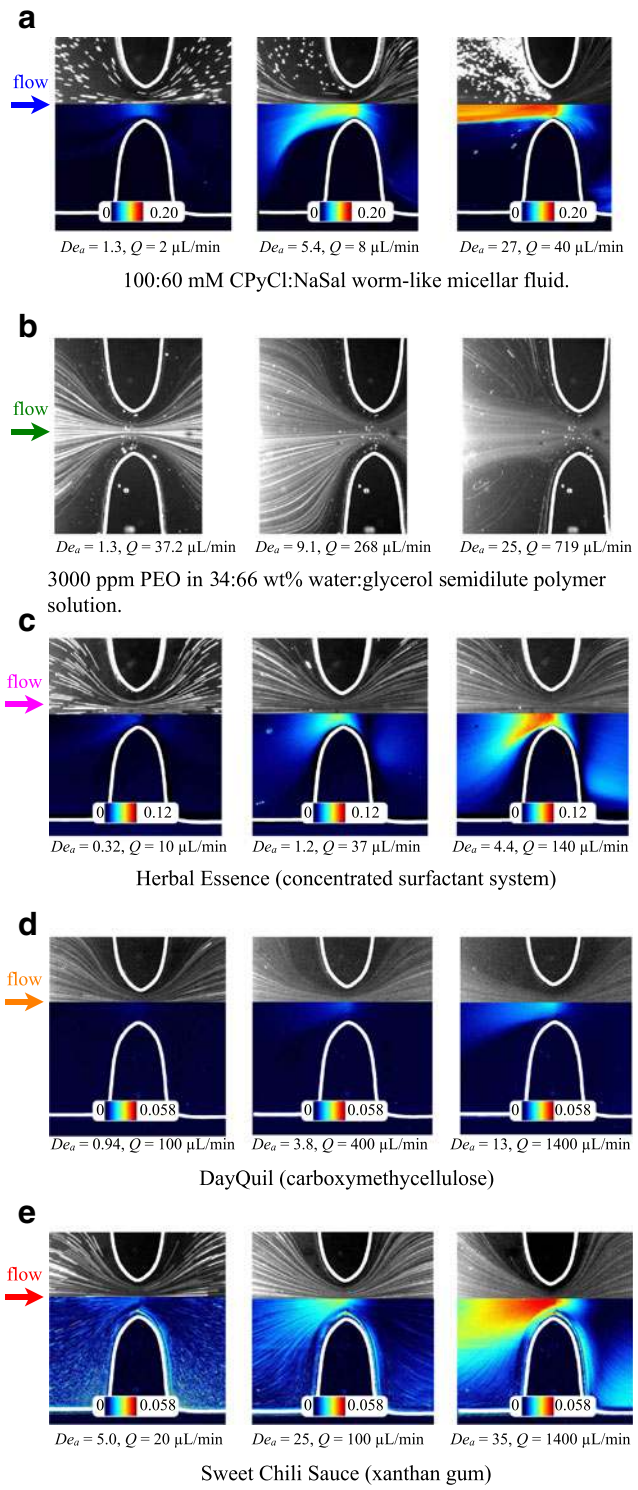

Fig. 9 Streakline images (*upper half*) and pseudocolor retardance maps (*lower half*) of flow-induced birefringence for non-Newtonian test fluids flowing through the hyperbolic contraction ($w_c = 400\ \mu$m). In all cases, the kinematics and retardance images are symmetrical about the contraction centerline and flow is from left to right. *White curves* have been overlaid to indicate the location of the contraction walls. The colorscale is in units of radians. Note that birefringence in the PEO solution was too weak to be observable and therefore no pseudocolor retardance images have been included

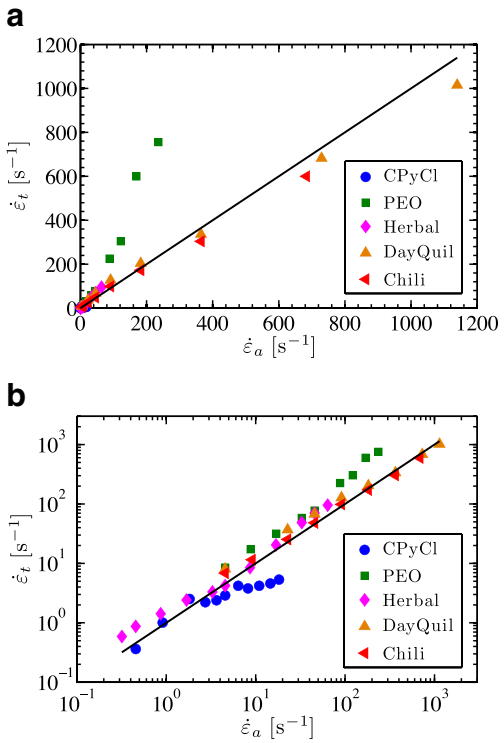

Fig. 10 True extension rate $\dot{\varepsilon}_t$ determined from the slope of the best linear fit $u_x = \dot{\varepsilon}_t x$ line to the measured centerline velocity near the contraction plane as a function of apparent extension rate $\dot{\varepsilon}_a$ given by Eq. (1). The *solid black line* indicates the ideal result of $\dot{\varepsilon}_t = \dot{\varepsilon}_a$. Note that the same data are displayed on (**a**) linear and (**b**) log scales

apparent value of $N_{1,a}$ shown in Fig. 8. We also note that although other micellar systems have been shown to exhibit irreversible flow-induced gelation in extension-dominated flows (Vasudevan et al. 2010), we have not observed the formation of any such permanent flow-induced structures with this surfactant system over the the range of Hencky strains and strain rates attained.

The superlinear increase in the apparent normal stress difference $N_{1,a}$ with $\dot{\varepsilon}_a$ for the PEO solution shown in Fig. 8 coincides with the measured rapid increase in the true extension rate $\dot{\varepsilon}_t$ with flow rate. Therefore, it is important to recognize that evidence for extensional thinning or thickening based on pressure measurements with EVROC, may in fact be indicative of the onset of viscoelastic secondary flows such as the upstream vortices seen in Fig. 9b. As with virtually every rheometer, it is a challenge with the EVROC to ensure that the flow kinematics remain self-similar and unchanged across all experimentally accessible flow rates, $\dot{\varepsilon}_a$. Accordingly this microfluidic device should not be viewed as a true extensional rheometer, *per se*, since the realized flow kinematics can vary with both the test fluid and the flow rate, even in the inertialess flow regime. Instead the EVROC device is best employed as a microfluidic viscosity indexer from which a semi-quantitative estimate of

the extensional rheology of the test sample can be ascertained in an extension-dominated flow at high deformation rates ($1 \leq \dot{\varepsilon}_a \leq 10^3\ \mathrm{s}^{-1}$).

Flow-induced birefringence and stress

Spatially resolved FIB measurements complement the streakline images by providing optically non-invasive measurements of local flow-induced molecular anisotropy. Pseudocolor retardance images at different flow rates are shown in the lower halves of each image in Fig. 9. Provided the optical anisotropy, Δn, (i.e., the difference between the ordinary and extraordinary indices of refraction) in the sample can be assumed constant along the direction of light propagation, then the optical retardance is given by $\delta = 2\pi\Delta n h/\lambda_\ell$, where h is the height of the contraction as before and $\lambda_\ell = 546$ nm is the wavelength of the incident light.

Under the appropriate circumstances, Δn can be related to the principal stress difference, $\Delta\sigma$, in the sample by the stress-optical rule, (Fuller 1990). This rule is given by the relation $\Delta n = C\Delta\sigma$, where C is the stress optical coefficient, which is typically determined experimentally (Janeschitz-Kriegl 1983). In a purely extensional flow, free from shear stresses, the principal stress difference is equal to the first normal stress difference, $\Delta\sigma = N_1$. Under the assumption of a purely two-dimensional, planar elongational deformation, and the applicability of the stress optical rule, the normal stress difference in the fluid is thus related to the measured optical retardance by the relationship

$$N_1 = \frac{\delta}{2\pi C}\frac{\lambda_\ell}{h} \tag{22}$$

In reality, the fluid kinematics are not uniform along the direction of light propagation (due to the presence of the bounding end walls), and therefore the retardance images in Fig. 9 are useful primarily for qualitatively assessing the stress field in the geometry. The retardance fields exhibit qualitatively similar trends as those seen in the flow kinematics measurements, especially with regard to the emergence of the upstream vortices which are characterized by slowly moving regions of low stress and low birefringence that appear dark blue in Fig. 9. It is also noteworthy that for flow rates large enough to produce detectable levels of birefringence, (typically $De_a > \mathcal{O}(1)$), the optical retardance does not exhibit fore-aft symmetry about the throat of the contraction (located at $x = l_c$), indicating the importance of tensile viscoelastic stresses as fluid elements are convected and stretched through the converging section of the contraction. Furthermore, for essentially all of the values of $\dot{\varepsilon}_a$ for which the flow is steady in time, the centerline retardance profile in the converging half of the contraction continues to grow monotonically with x-position as fluid elements travel towards the throat of the contraction $x \rightarrow l_c$. This result suggests that the Hencky strain for this channel, $\varepsilon_H = 2$, is not sufficiently large to provide sufficient time for the extensional stress in the fluid element to attain its steady state value. This was a central assumption of the energy analysis presented in Eq. 20–21 and thus provides an *a posteriori* rationalization for the fact that only an approximate value of the planar extensional viscosity can be measured with a hyperbolic microfluidic device such as EVROC that develops a Hencky strain $\varepsilon_H = 2$.

Conclusions

In this study, the extensional flows of a range of Newtonian and non-Newtonian fluids through a microfluidic hyperbolic contraction have been studied using local pressure field measurements, kinematic measurements (using μ-PIV and streakline imaging) and full-field FIB measurements. We have shown that this device can be used for indexing and comparing the behavior of a wide range of complex fluids in an extension-dominated flow; however, careful measurements of both the pressure field and flow kinematics are important for accurate interpretation of the results.

For the flows of Newtonian liquids at low Reynolds number, $Re_0 < \mathcal{O}(10)$, the measured pressure drop across the contraction, ΔP_{23}, increases linearly with apparent extension rate $\dot{\varepsilon}_a$. Furthermore, provided one accounts for the position of the MEMS transducers, one can estimate the pressure drop across the contraction alone, ΔP_c, which can be predicted using a 2D lubrication approximation for viscous Newtonian flow to within a constant numerical factor of around three. This residual discrepancy can be attributed to the inadequacy of a 2D approximation in capturing a truly 3D flow within this shallow microfludic device, as well as additional complicating effects arising from the geometric abruptness of the contraction and the non-rectangular cross-section of the contraction region (caused by the wet etching fabrication process).

Flow velocimetry measurements confirm that the hyperbolic contraction imposes an extension rate along the centerline that is approximately uniform spatially, but roughly 66 % larger than the nominal value, $\dot{\varepsilon}_t \approx 1.66\dot{\varepsilon}_a$, based on a least squares linear fit to the measured extension rates. These measurements also reveal the onset of initial extensional effects as much as three contraction lengths upstream of the contraction entrance as a result of the abruptness of the hyperbolic contraction. These non-idealities in the extensional flow kinematics are the cause of the larger than anticipated pressure drop based on the lubrication approximation. We have recently shown (for an alternative cross-slot extensional flow configuration), however, that the extensional kinematics can be optimized with numerical

simulations (Haward et al. 2012b). Accordingly, we plan to use similar numerical kinematic optimization simulations to further enhance the capabilities of the EVROC microfluidic extensional viscometer in future studies.

Two model viscoelastic liquids and three commercially available complex fluid formulations have been tested in the EVROC. For viscoelastic materials it is assumed that the pressure drop in the contraction, ΔP_c, is a superposition of a pressure drop due to viscous shear stresses, ΔP_v, and an extra pressure drop due to elastic stresses, ΔP_e, hence $\Delta P_c = \Delta P_v + \Delta P_e$. The value of ΔP_v is estimated using a 2D lubrication analysis for a power-law fluid and the remaining elastic contribution to the pressure drop ΔP_e is used to calculate an apparent extensional viscosity $\eta_{E,a}$. Typical Trouton ratios when referenced to the zero-shear-rate viscosity are $\mathcal{O}(10)$, but the values of this ratio should not be interpreted as a true Trouton ratio measured in homogeneous extensional flow, since the flow through this contraction has mixed shear and extensional components.

Flow velocimetry measurements and streakline images demonstrate that typically for $De_a < \mathcal{O}(1)$ the flow field remains largely unchanged from the low Reynolds number flow field expected for a Newtonian fluid in a planar hyperbolic contraction, with the experimentally-realized extension rate along the contraction centerline proportional to the flow rate. For $De_a > \mathcal{O}(1)$, an elastically-driven secondary flow emerges which results in upstream vortex growth and undermines any assumption of a self-similar, Newtonian-like flow. However the experimentally-measured kinematics along the contraction centerline show that the extension rate is still spatially homogeneous for a given flow rate and that useful measurements can still be made in this regime. Above a higher critical Deborah number, $De_a > \mathcal{O}(10)$, the flow becomes time-varying and reliably extracting $\eta_{E,a}(\dot{\varepsilon})$ from the measured pressure drop is difficult. Full-field measurements of flow-induced birefringence generally confirm the qualitative features seen in the streakline images, whilst also showing that the local state of tensile stress in the fluid is still evolving as it flows towards the contraction throat.

In summary, this microfluidic hyperbolic contraction device can be used to investigate the extensional viscosity of a complex fluid such as an ink or liquid foodstuff or consumer product up to extension rates $\dot{\varepsilon}_a \sim \mathcal{O}(10^3)$ s^{-1} using the following steps:

(i) A series of steady pressure drop measurements through the device are made as a function of imposed flow rate (*cf.* Figs. 4 and 6).

(ii) The pressure coefficient $\mathcal{P} \equiv \Delta P_{23}/\Delta P_{14}$ can be calculated as a measure of the relative importance of viscoelastic effects to the total pressure drop. This value should approach unity, $\mathcal{P} \to 1$, as viscoelastic effects become increasingly dominant (*cf.* Fig. 7a).

(iii) The pressure drop ΔP_c across the contraction is calculated from Eq. 3 and the apparent extensional rate for each flow rate is calculated from Eq. 1 (*cf.* Fig. 7b).

(iv) The viscoelastic contribution to the pressure drop ΔP_e can be calculated using the equation $\Delta P_e = \Delta P_c - \Delta P_v$, where ΔP_v can be estimated from Eq. 17. The apparent extensional viscosity $\eta_{E,a}$ can then be determined using Eq. 21.

(v) If desired, a second transparent microfluidic chip can be used to measure the local kinematics and optical retardance with full-field μ-PIV and birefringence measurements as illustrated in Fig. 9. Such measurements can be valuable in ascertaining that the planar elongational flow is stable and the kinematics are homogeneous.

This hyperbolic planar contraction can serve as a complement to the shear viscosity microfluidic viscometer described in Pipe et al. (2008) for measuring a nominal extensional viscosity. The combination of measurements obtained with these two devices will be valuable to an applied rheologist for quality control monitoring (i.e., indexing variations in the extensional rheology of a specific fluid formulation) as well as for providing a simple and quick evaluation of the performance of a particular viscoelastic fluid in filling and dispensing applications featuring converging nozzles that are characterized by high shear and extension rates.

Acknowledgments The authors wish to acknowledge Dr. Seong-Gi Baek and Dr. Ying-Chih Wang of RheoSense, Inc. for material support in the form of the EVROC chips and associated hardware. We also are grateful to Dr. Mónica Oliveira, Dr. Trushant Majmudar and Dr. Vivek Sharma for helpful discussions. TJO acknowledges the NSF Graduate Research Fellowship for funding. SJH acknowledges funding from NASA Microgravity Fluid Sciences (grant NNX09AV99G) and the European Commission under Marie Curie action FP7-PEOPLE-2011-IIF (grant 298220).

References

Adams EB, Whitehead JC, Bogue DC (1965) Stresses in a viscoelastic fluid in converging and diverging flow. AIChE J 11(6):1026–1032

Afonso AM, Oliveira PJ, Pinho FT, Alves MA (2011) Dynamics of high-Deborah-number entry flows: a numerical study. J Fluid Mech 677:272–304

Aguayo JP, Tamaddon-Jahromi HR, Webster MF (2008) Excess pressure-drop estimation in contraction and expansion flows for constant shear-viscosity, extension strain-hardening fluids. J Non-Newtonian Fluid Mech 153(2–3):157–176

Baek SG, Magda JJ (2003) Monolithic rheometer plate fabricated using silicon micromachining technology and containing miniature pressure sensors for N_1 and N_2 measurements. J Rheol 47(5):1249–1260

Bandalusena HCH, Zimmerman WB, Rees JM (2009) Microfluidic rheometry of a polymer solution by micron resolution particle image velocimetry: a model validation study. Meas Sci Technol 20(11):115404

Bandalusena HCH, Zimmerman WB, Rees JM (2010) Creeping flow analysis of an integrated microfluidic device for rheometry. J Non-Newtonian Fluid Mech 165(19–20):1302–1308

Binding DM, Walters K (1988) On the use of flow through a contraction in estimating the extensional viscosity of mobile polymer solutions. J Non-Newtonian Fluid Mech 30(2–3):233–250

Bird RB, Armstrong RC, Hassager O (1987) Dynamics of polymeric liquids, Vol 1, 2nd edn. Wiley, New York

Cates ME, Fielding SM (2006) Rheology of giant micelles. Adv Phys 55(7–8):799–879

Cogswell FN (1972) Converging flow of polymer melts in extrusion dies. Polym Eng Sci 12(1):64–73

Cogswell FN (1978) Converging flow and stretching flow: a compilation. J Non-Newtonian Fluid Mech 4(1–2):23–38

Collier JR, Romanoschi O, Petrovan S (1998) Elongational rheology of polymer melts and solutions. J Appl Polym Sci 69:2357–2367

Dubash N, Cheung P, Shen AQ (2012) Elastic instabilities in a microfluidic cross-slot flow of wormlike micellar solutions. Soft Matter 8:5847–5856

Everage AE, Ballman RL (1978) The extensional flow capillary as a new method for extensional viscosity measurement. Nature 273(5669):213–215

Feigl K, Tanner FX, Edwards BJ, Collier JR (2003) A numerical study of the measurement of elongational viscosity of polymeric fluids in a semihyperbolically converging die. J Non-Newtonian Fluid Mech 115:191–215

Ferer M, Anna SL, Tortora P, Kadambi JR, Oliver M, Bromhal GS, Smith DH (2011) Two-phase flow in porous media: predicting its dependence on capillary number and viscosity ratio. Transp Porous Med 86(1):273–289

Fuller GG (1990) Optical rheometry. Annu Rev Fluid Mech 22:387–417

Galindo-Rosales FJ, Alves MA, Oliveira MSN (2013) Microdevices for extensional rheometry of low viscosity elastic liquids: a review. Microfluid Nanofluid 14(1–2):1–19

Groisman A, Quake SR (2004) A microfluidic rectifier: anisotropic flow resistance at low Reynolds numbers. Phys Rev Lett 92(9):094501

Han CD, Drexler LH (1973a) Studies of converging flows of viscoelastic polymeric melts. 1. Stress-birefringent measurements in entrance region of a sharp-edged slit die. J Appl Polym Sci 17(8):2329–2354

Han CD, Drexler LH (1973b) Studies of converging flows of viscoelastic polymeric melts. 3. Stress and velocity distributions in entrance region of a tapered slit die. J Appl Polym Sci 17(8):2369–2393

Hashimoto T, Kido K, Kaki S, Yamamoto T, Mori N (2006) Effects of surfactant and salt concentrations on capillary flow and its entry flow for wormlike micelle solutions. Rheol Acta 45(6):841–852

Haward SJ, McKinley GH (2012) Stagnation point flow of wormlike micellar solutions in a microfluidic cross-slot device: effects of surfactant concentration and ionic environment. Phys Rev E 85:031502

Haward SJ, Ober TJ, Oliveira MSN, Alves MA, McKinley GH (2012a) Extensional rheology and elastic instabilities of a wormlike micellar solution in a microfluidic cross-slot device. Soft Matter 8(2):536–555

Haward SJ, Oliveira MSN, Alves MA, McKinley GH (2012b) Optimized cross-slot flow geometry for microfluidic extensional rheometry. Phys Rev Lett 109(12):128301

Hudson SD, Phelan FR Jr, Handler MD, Cabral JT, Migler KB, Amis EJ (2004) Microuidic analog of the four-roll mill. Appl Phys Lett 85(2):335–337

James DF, Saringer JH (1982) Flow of dilute polymer solutions through converging channels. J Non-Newtonian Fluid Mech 11:317–339

James DF (1991) Flow in a converging channel at moderate Reynolds-numbers. AIChE J 37(1):59–64

Janeschitz-Kriegl H (1983) Polymer melt rheology and flow birefringence. Springer-Verlag, New York

Kang K, Koelling KW, Lee LJ (2006) Microdevice end pressure evaluations with Bagley correction. Microfluid Nanofluid 2(3):223–235

Lee JS, Dylla-Spears R, Teclemariam NP, Muller SJ (2007) Microfluidic four-roll mill for all flow types. Appl Phys Lett 90(7):074103

Lerouge S, Berret J-F (2010) Shear-induced transitions and instabilities in surfactant wormlike micelles. In: Dusek K, Joanny J-F (eds) Polymer characterization of advances in polymer science, vol 230. Springer, Berlin, pp 1–71

Marín-Santibáñez BM, Pérez-González J, de Vargas L, Decruppe JP, Huelsz G (2009) Visualization of shear banding and entry Poiseuille flow oscillations in a micellar aqueous solution. J Non-Newtonian Fluid Mech 157(1–2):117–125

Masselon C, Salmon JB, Colin A (2008) Nonlocal effects in flows of wormlike micellar solutions. Phys Rev Lett 100(3):038301

McKinley GH, Tripathi A (2000) How to extract the Newtonian viscosity from capillary breakup measurements in a filament rheometer. J Rheol 44(3):653–670

Meinhart CD, Wereley ST, Gray MHB (2000) Volume illumination for two-dimensional particle image velocimetry. Meas Sci Technol 11(6):809–814

Nyström M, Tamaddon-Jahromi HR, Stading M, Webster MF (2012) Numerical simulations of Boger fluids through different contraction configurations for the development of a measuring system for extensional viscosity. Rheol Acta 51:713–727

Ober TJ, Soulages J, McKinley GH (2011) Spatially resolved quantitative rheo-optics of complex fluids in a microfluidic device. J Rheol 55(5):1127–1159

Oliveira MSN, Alves MA, Pinho FT, McKinley GH (2007) Viscous flow through microfabricated hyperbolic contractions. Exp Fluid 43(2–3):437–451

Oliveira MSN, Rodd LE, McKinley GH, Alves MA (2008) Simulations of extensional flow in microrheometric devices. Microfluid Nanofluid 5(6):809–826

Pandey A, Lele A (2007) Exploring the utility of an axisymmetric semi-hyperbolic die for determining the transient uniaxial elongation viscosity of polymer melts. J Non-Newtonian Fluid Mech 144:170–177

Pathak JA, Hudson SD (2006) Rheo-optics of equilibrium polymer solutions: Wormlike micelles in elongational flow in a microfluidic cross-slot. Macromolecules 39(25):8782–8792

Pipe CJ, Majmudar TS, McKinley GH (2008) High shear rate viscometry. Rheol Acta 47(5–6):621–642

Pipe CJ, McKinley GH (2009) Microfluidic rheometry. Mech Res Commun 36(1):110–120

Rajagopalan D (2000) Computational analysis of techniques to determine extensional viscosity from entrance flows. Rheol Acta 39:138–151

Rodd LE, Scott TP, Boger DV, Cooper-White JJ, McKinley GH (2005) The inertio-elastic planar entry flow of low-viscosity elastic fluids in micro-fabricated geometries. J Non-Newtonian Fluid Mech 129(1):1–22

Rodd LE, Cooper-White JJ, Boger DV, McKinley GH (2007) Role of the elasticity number in the entry flow of dilute polymer solutions

in micro-fabricated contraction geometries. J Non-Newtonian Fluid Mech 143:170–191

Schuberth S, Münstedt H (2008) Transient elongational viscosities of aqueous polyacrylamide solutions measured with an optical rheometer. Rheol Acta 47(2):139–147

Sousa PC, Pinho FT, Oliveira MSN, Alves A (2011) Extensional flow of blood analog solutions in microfluidic devices. Biomicrofluidics 5:014108

Sousa PC, Pinho FT, Oliveira MSN, Alves MA (2012) High performance microfluidic rectifiers for viscoelastic fluid flow. RSC Adv 2(3):920–929

Stone PA, Hudson SD, Dalhaimer P, Discher DE, Amis EJ, Migler KB (2006) Dynamics of wormlike micelles in elongational flows. Macromolecules 39(20):7144–7148

Tamaddon-Jahromi HR, Webster MF, Aguayo JP, Manero O (2011) Numerical investigation of transient contraction flows for wormlike micellar systems using Bautista–Manero models. J Non-Newtonian Fluid Mech 166(1–2):102–117

Vasudevan M, Buse E, Lu D, Krishna H, Kalyanaraman R, Shen AQ, Khomami B, Sureshkumar R (2010) Irreversible nanogel formation in surfactant solutions by microporous flow. Nat Mater 9(5):436–441

Wang J, James DF, Park CB (2010) Planar extensional flow resistance of a foaming plastic. J Rheol 54(1):95–116

Wang J, James DF (2011) Lubricated extensional flow of viscoelastic fluids in a convergent microchannel. J Rheol 55(5):1103–1126

White FM (2006) Viscous fluid flow, 3rd edn. McGraw-Hill, New York